Philippine e-Journal for Applied Research and Development 10(2020), 1-13 ISSN 2449-3694 (Online)
http://pejard.slu.edu.ph/vol.10/2020.05.15.pdf

Electrochemical Properties of Synthesized Fe-doped Amorphous SiO_2 as Anode Material for Lithium Batteries

Maricris C. Cunanan[1,*], Benjamin Jose C. Alfaro[1], Jimyl Arabit-Cruz[1], Christian C. Vaso[1], Jey-R S. Ventura[1] and Rinlee Butch M. Cervera[2]

[1]Department of Engineering Science, College of Engineering and Agro-Industrial Technology, University of the Philippines Los Baños, College, 4031 Los Baños, Laguna
[2]Department of Mining, Metallurgical and Materials Engineering, College of Engineering, University of the Philippines Diliman, 1101 Diliman, Quezon City
** Corresponding author (mccunanan@up.edu.ph)*

Received, 4 February 2020; Accepted, 29 April 2020; Published, 15 May 2020

Abstract

Lithium-ion batteries (LIBs) with anodes fabricated using an alloy of silica (SiO_2) and lithium have increased capacity to store energy. SiO_2 derived from cheap sources like rice hull (RH) can be doped with a metallic compound to increase its performance. In this study, SiO_2 extracted from RH via acid precipitation was doped with varying percentages of iron (Fe) at different calcination temperatures. Various analysis techniques were employed to investigate the micro and physical structure of the synthesized SiO_2. Electrochemical characterization of the samples calcined at 800°C revealed higher open-circuit values (OCV), lithiation and delithiation capacity, and Coulombic efficiency than those calcined at 400°C. Higher OCV and lithiation and delithiation capacity were obtained from samples with 5%-dopant compared to those with 10%-dopant. Highest OCV, lithiation and delithiation capacities obtained from the samples calcined at 400°C with 5%-dopant were 2.916V, 959.52 $mAh \cdot g^{-1}$, and 238.58 $mAh \cdot g^{-1}$, respectively.

Keywords: energy storage devices, silica from rice hull, acid precipitation, electrochemistry, nanosilica

Introduction

The demand for efficient energy storage devices has been on the rise due to the widespread development of electronic gadgets and electric vehicles. While there are a number of alternative and renewable energy sources like biofuels, natural gas, hydroelectric, wind, wave, and solar; storage devices with high capacity for energy play a key role in making these sources usable for consumers (Manthiram, 2009).

Batteries are the primary energy storage devices. The amount of energy stored per unit volume or per unit weight, also known as energy density, is largely dependent on the capacity of the battery cell. Compared with other high energy density storage systems like lead–acid, nickel–cadmium, and nickel–metal hydride batteries; lithium-ion batteries (LIBs) exhibit the highest energy density (Manthiram, 2009) and thus have been receiving much attention from the research community (Wu et al., 2019). Aside from their high energy density, LIBs present other advantages like lack of memory effect, rapid charge/discharge rate, low pollution and working voltage, long cycle life (>500 cycles)

and low self-discharge property (<10% per month at 21°C). They are also fairly maintenance-free, very lightweight compared to traditional lead-acid and Ni-based batteries, and have good environment compatibility (Liu et al., 2010).

Previously, LIBs utilized graphite as their anode (Bhanvase & Pawade, 2018). Among the advantages of graphite materials are stable specific capacity, small irreversible capacity (Liu et al., 2010), long discharge/charge voltage platform, good cycling performance, and low cost (Ma et al., 2015). Thus, commercial electrochemical-grade graphite delivers stable capacity over several hundred cycles due to low volume change and low stress (Li, 2012).

Any lithium-based carbonous material, Li_xC_6, has a limited intercalate stoichiometry due to its volumetric (840 $mAh \cdot mL^{-1}$) and specific capacity (372 $mAh \cdot g^{-1}$) that are relatively low compared to Li metal (3800 $mAh \cdot g^{-1}$) (Mukanova et al., 2002). However, Li metal cannot be used due to its poor recharge ability in common electrolytes. Thus, attention has shifted to Li alloys involving elements such as tin (Sn), antimony (Sb), silicon (Si), and germanium (Ge) to deliver a higher anode capacity (Park et al., 2010; Ma et al., 2014). Among the mentioned elements, Li-Si electrodes give the highest gravimetric capacity (4200 mAh g^{-1}) and volumetric capacity (2400 mAh cm^{-1}) (Ma et al., 2014). Li-Si electrodes store ten times more Li than graphite and allow for a higher energy density on the anode. This is because four Li atoms can attach to one silicon atom (Liu et al., 2011; Jin et al., 2017). Another advantage of silicon-based alloys is their low-cost, non-toxic, safe, and stable nature (Park et al., 2010; Ma et al., 2014).

However, the application of bulk silicon anode faces some major problems. Large volume change of Li–Si alloy during Li insertion and extraction invariably generates great mechanical stresses in the brittle silicon lattice, leading to electrode cracking and electrical disconnection between the active materials and the current collector (Zhang et al., 2012; Zhao et al., 2012). The resulting loss of connectivity with the conducting additive particles leads to poor storage capability and fast capacity fading (Wen et al., 2013). Another significant challenge is attaining a long life cycle for silicon anodes, which are limited to just hundreds of cycles due to material pulverization during cycling and unstable solid electrolyte interface (SEI) layers (Jin et al., 2017).

Aside from metallic Si, Si-based oxides (SiO_x) can also be used as anode materials. As SiO_x reacts with lithium, lithium oxides and silicates are produced. These products form a buffer layer that permits large volume changes of the Si and ease the development of stable SEI layers (Dai et al., 2012). The problem on volume expansion of Li-Si electrodes can also be addressed by nanosizing Si-based oxides; this increases their porosity and surface area and thus increasing their functionality. Moreover, internal pores can accommodate volume expansion without damaging the SEI (Dai et al., 2012; Liu et al., 2013; Cervera et al., 2014; Favors et al., 2014).

Nanostructured silica and its derivatives can be sourced from rice husk or rice hull (RH), an agricultural by-product produced annually at a rate of 1.2×10^8 tons worldwide (Liu et al., 2013). Because of its high porosity and surface area, silica from RH has been reported to have improved the properties of materials (Liou et al., 2011; Hossain et al., 2018). Nanosilica particles were used as additives in fabricating superhydrophobic nanocomposite coatings, which exhibited stability and durability against disintegration through time and improved anti-corrosion functionality even when exposed to a corrosive environment (Caldona et al., 2017; Caldona et al., 2019). Likewise, incorporating nanosilica particles in nanofluids has improved the base fluid performance, thus indicating potential for solar, automobile, electronic cooling, and biomedical applications (Ong et al., 2019). The contributions of nanosilica in the improved properties of various materials may also prove valuable in increasing the performance of LIB materials.

A few studies have investigated the various ways that RH can be used as raw material for anodes. Cui et al. (2017) synthesized micro-sized porous C/SiO_2 through carbonization process. Ju et al. (2016) converted RH to SiO_x/C composite material directly by heat treatment under argon/hydrogen atmosphere. Kim et al. (2017) produced mesoporous Si by reducing SiO_2 from RH using a magnesio-milling process. These reports explore the use of amorphous silica (AnS) from rice hull

because AnS is more reactive to lithiation than crystalline silica due to its lower density that provides free spaces for Li atoms (Chang et al., 2012).

This study utilizes AnS from rice hull following the procedure of Mirasol & Cervera (2015). The AnS produced is synthesized via acid precipitation and doped with Fe to increase its conductivity. The anode performance of the synthesized sample is investigated, as well as its electrochemical properties such as open-circuit voltage, specific capacity, Coulombic efficiency (CE), cyclability and charge/discharge rate. A previous study (Garrido & Cervera, 2015) produced Fe-doped AnS-based anode material, via low temperature sol-gel method, but not from rice hull. Hence, this is the first account that introduces the use of actual Fe-doped RH SiO_2 anode material on the improvement of lithium-based batteries.

Materials and Methods

SiO_2 Processed from RH via Acid Precipitation

Approximately 125.0 g of as-received Philippine RH (variety: PSB Rc-18, harvested in Ilocos Norte in 2013 during the wet season) was screened and washed with tap water to remove the adhering soil and contaminants, and then dried in an oven at 120°C for 4 h (Mirasol & Cervera, 2015). The cleaned sample was then thermally treated using a non-programmable electric furnace heated at 500°C for 2.5 h. Afterwards, it was subjected to another 3-h heating at 550°C using a muffle furnace to obtain approximately 17.0 g of bulk SiO_2 ash.

The SiO_2 ash obtained was leached using 1 M HCl to remove metallic impurities. Subsequent extraction of sodium silicate solution was carried using 2.5 M NaOH followed by gradual thermal treatment up to 650°C for 2 h to finally yield AnS. Since the obtained AnS is generally considered an electrochemically inactive material for LIBs, it was doped with 5 mol% and 10 mol% Fe: stoichiometric amounts of 95% pure Fe(II) acetate (Sigma-Aldrich, USA) were mixed with 2.5 g AnS and ground together in an agate mortar and pestle for 30 min to ensure a homogenous mixture. One batch each of 5%- and 10%-doped samples were then calcined in a furnace at 400°C for 1 h, and a second batch at 800°C for 2 h. The final samples were labelled as 5%400RH, 10%400RH, 5%800RH and 10%800RH.

Characterization of Synthesized Samples

Thermogravimetric analysis (TGA) with simultaneous differential thermal analysis (TG-DTA) of the oven dried rice hull (as-dried RH) were carried out on a STA 6000 Perkin Elmer (Massachusetts, USA) thermogravimetric analyzer with a scan rate of 10°C/min under nitrogen atmosphere at a flow rate of 50 cm^3/min. The temperature range was from 30-950°C.

X-ray diffraction (XRD) analysis of the synthesized samples were performed on a Shimadzu MAXima XRD-7000 (Tokyo, Japan) diffractometer with a monochromic copper Kα (λ = 1.54 Å) radiation source scanned at a rate of 2°/min in the 3–90° range. The XRD analysis was conducted at a voltage of 40 kV and a current intensity of 30 mA. Fourier transform infrared (FTIR) analysis, meanwhile, was performed using a Nicolet™ iS50 FTIR Spectrometer (Madison, USA) with a resolution of 16 cm^{-1}. Each sample was analyzed for 30 sec using a scan range of 400-4000 cm^{-1}.

The scanning electron microscopy (SEM) images and SEM-Energy dispersive x-ray spectroscopy (SEM-EDS) were acquired from a JEOL JSM 5310 (Tokyo, Japan) scanning microscope. To improve the imaging of the non-conductive samples, all were sputter coated with a thin layer (~ 3 nm) of gold particles. The 5%-doped and 10%-doped samples were then processed at an accelerating voltage of 15 kV and 20 kV, respectively.

Particle size analysis via Dynamic Light Scattering (DLS) using the mean values, D10, D50, D90, and distribution widths were carried out using the NanoPlus1 Particle Size and Zeta Potential Analyzer from Micromeritics Particulate Systems (Georgia, USA). Prior to processing, the samples were dispersed in ethanol at 0.1 g/10 mL concentration and ultrasonicated for 10 min. A drop of sodium tripolyphosphate was also used as a dispersing additive.

Electrode Preparation and Cell Assembly

Electrochemical tests were carried out using either a Swagelok-type or CR2032-type coin cell assembled in an argon-filled (99.9% purity) glove box (<100 ppm O_2 and H_2O levels) using a two electrode set-up. To prepare the electrodes, each of the four doped powders were homogenized for 30 min with carbon black (conducting additive) and polyvinylidene difluoride (PVDF) binder using an agate mortar and pestle in a 70:20:10 wt% ratio. To create the working electrode, the black powder mixture produced was pressed on a steel mesh (0.149 mm) for 3 min at 10 kPa and cured in an oven at 150°C for 1 h. Li foil was used as a counter electrode. The working and counter electrodes were separated by 2 layers of Hipore ND525 (Tokyo, Japan) polyolefin separator that has a diameter of $^{15}/_{16}$ inch and $^{11}/_{16}$ inch for the Swagelok and coin cell, respectively. 1 M $LiPF_6$ dissolved in a mixture of 1:1 (v/v) ethylene carbonate and dimethyl carbonate was used as electrolyte.

Electrochemical Characterization

Electrochemical performance of the cells was tested at ambient temperatures using VMP300 (Biologic, France) multi-channel potentiostat/galvanostat and analyzed using ECLab® software. For the synthesized Fe-doped samples, first cycle Galvanostatic charge-discharge (GCD) was done in the range of 0-2 V at a constant current of 0.05 mA. The theoretical specific GCD capacity of SiO_2 of 1,779.38 $mAh \cdot g^{-1}$ (Mirasol & Cervera, 2015) was used to obtain the experimental capacity of the samples. Since the C-rate depends on the weight ratio of the active material (the synthesized powder) in the anode mixture, all samples had different C-rate values and, consequently, varying service times for charging and discharging. The samples which reported the highest CE and best specific capacity were further subjected to GCD testing at two other C-rates (C/20 and C/100).

Results and Discussion

SiO_2 Processed from RH via Acid Precipitation

Figure 1 shows the changes in appearance and color of the as-received RH (Figure 1a) as it was synthesized to become AnS. From the orange hue of RH, it became black strands of SiO_2 ash (Figure 1b) that turned gray after heating at 550°C (Figure 1c). It then became pure white with subsequent acid leaching, silicate extraction and titration (Figure 1d).

Characterization of SiO_2 from RH

The stacked simultaneous TG-DTG-DTA curve of dried RH in Figure 2 shows a total

Figure 1. Optical image of (a) raw RH, (b) SiO_2 calcined at 500°C, (c) SiO_2 calcined at 550°C, and (d) synthesized RH SiO_2.

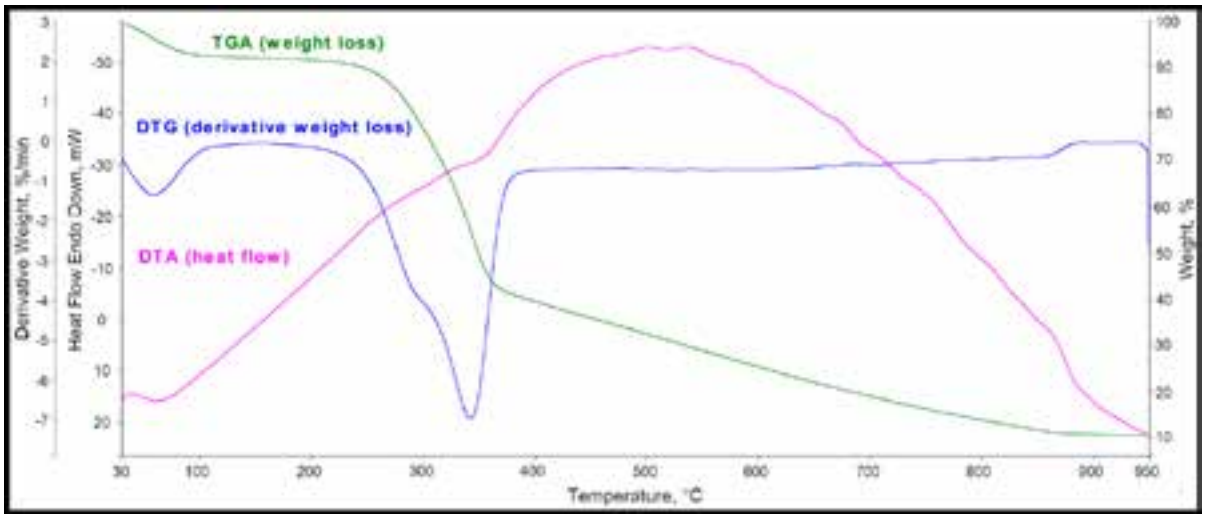

Figure 2. TG-DTG-DTA curves for as-dried RH.

Table 1. TG-DTG data of as-dried RH.

Stage	Weight Loss, %	Temp Range, °C	Reaction
I	7.32	30 –200	Removal of Physisorbed and Chemisorbed H_2O
II	52.37	200-400	Release of Volatile Matter
III	28.57	400-900	Combustion Process

weight loss of 88.97%. The curve indicates that significant weight loss occurred in three stages (Table 1), namely: (I) removal of moisture (7.32%) from 30-200°C, (II) breakdown of cellulose, hemicellulose, and lignin (52.37%) at 200-400°C, and (III) burning of carbonous residues and other combustibles (28.57%) at 400-900°C.

The thermal analysis presented in Table 1 is similar to the results of Chakraverty et al. (1985). Genieva et al. (2008) reported that the hemicellulose and cellulose components of RH, which comprises approximately 18-21% and 25-35% of RH, respectively, were the main sources of the evolution of volatile compounds. Lignin, 26-31% of RH, is mainly responsible for the charred portion of the product. Hemicellulose is degraded first at a temperature range of 150-350°C, while cellulose and lignin degrade at 275-350°C and 250-500°C, respectively (Yin & Goh, 2011). Since RH is composed of 30-50% of organic carbon (Phonphuak & Chindaprasit, 2015), the 28.57% weight loss at 400-900°C can be attributed to the combustion of this component.

The three stages during heating were confirmed by the endothermic peaks (59.44°C, 341.98°C and 859.73°C) in the DTA graph. An extra 4th peak at 500-540°C can be attributed to the melting of silica catalyzed by metal impurities in raw RH and the formation of bulk SiO_2 (Liu et al., 2013).

The XRD patterns of the synthesized samples from RH shown in Figure 3 reveals a combination of amorphous and crystalline peaks. All spectra show distinct broad bands at ~22.5° that are characteristic of amorphous silica (Ferreira et al., 2015). The additional peaks may be attributed to the formation of some crystalline SiO_2 phases such as tridymite (2θ = 23°, 43, 64°), quartz (2θ = 55°), coesite (2θ = 34°, 45°, 50°) and cristobalite (2θ = 32°, 54°) (Musić et al., 2011; Adams et al., 2013; Garrido & Cervera, 2015).

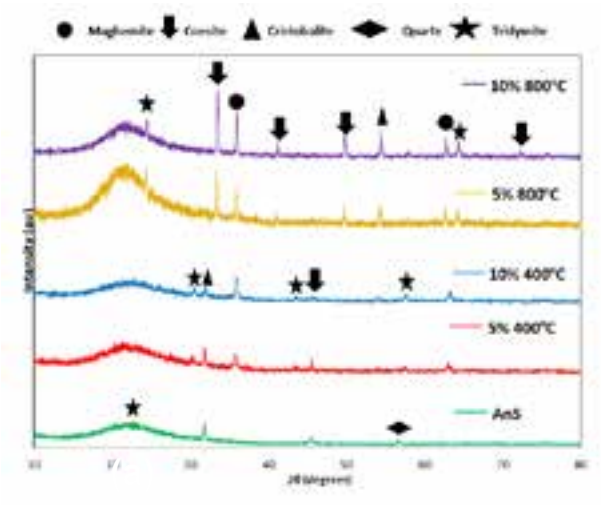

Figure 3. Stacked XRD spectra of the synthesized pure and Fe-doped SiO_2 samples from RH calcined 400°C and 800°C.

Common to both doped samples are the diffraction peaks at ~36° and ~63° that can be attributed to the formation of low-crystallinity γ-Fe_2O_3 (maghemite) nanoparticles. The increased intensity and narrow peak width indicates the increase of Fe concentration (Garrido & Cervera, 2015). Since the diffraction peaks are relatively higher in the samples calcined at 800°C than in samples calcined at 400°C, crystal growth and formation of large clusters are more apparent in the former.

The FTIR spectra of the as-prepared and synthesized samples from RH are presented in Figure 4. Common to all are the three characteristic absorption bands arising from Si-O-Si groups (Bansal et al., 2006; Wang et al., 2011). The lowest frequency band at about 460 cm^{-1} is caused by the Si-O-Si rocking mode which corresponds to the out of plane motion of the oxygen atom. The weakest absorption of intermediate frequency at approximately 800 cm^{-1} is connected with bending vibrations in which the oxygen atom motion occurs in the Si-O-Si plane and along the Si-O-Si angle bisector. The absorption peak at 1020–1110 cm^{-1} is assigned to the Si-O-Si asymmetric stretching vibration. The intense band at 1047 cm^{-1} is related to the stretching vibrations of silicon-oxygen tetrahedrons while the relatively weak absorption band at 795 cm^{-1} is most likely linked to the symmetric and asymmetric vibrations of the Si−O bonds in the silicon-oxygen network (Prado & Spinacé, 2015). Also, notice the almost similar FT-IR spectra of leached silica, bulk silica and AnS, indicating that the pre-treatment does not affect the chemical structure of the synthesized silica (Wang et al., 2011).

The broad peak at 3,200–3,600 cm^{-1} of the samples calcined at 400°C corresponds to the stretching vibrations of hydroxyl groups (Figure 4b). The absence of this peak in the spectra of the samples calcined at 800°C therefore indicates purity of SiO_2 and rice hull. The band at 1,630–1,640 cm^{-1} denotes the deformation mode of water molecules absorbed on the silica particle surface. The stretch in the 3700 cm^{-1} to 3400 cm^{-1} band is attributed to the presence of Si-OH and H-OH bonds (Caldona et al., 2019).

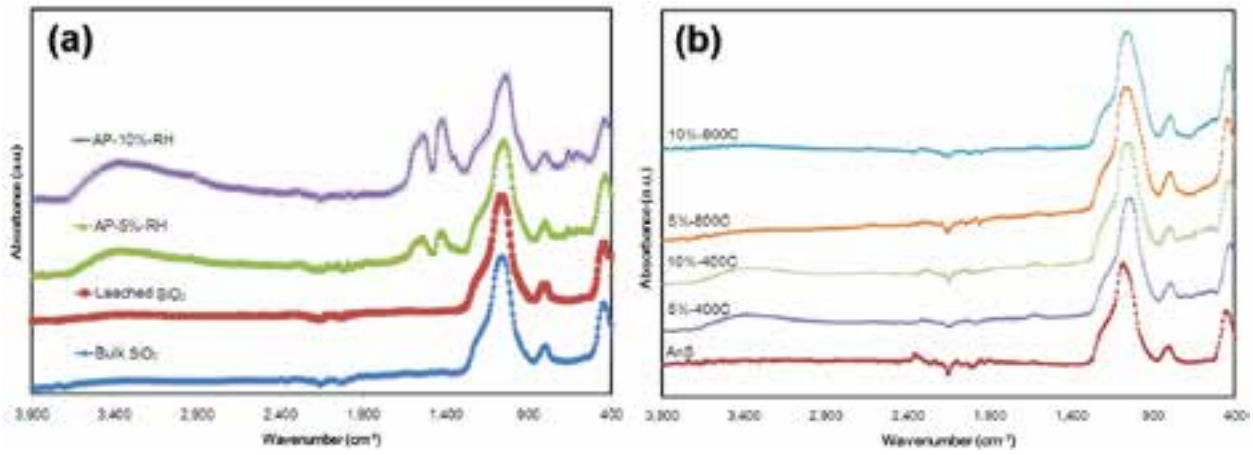

Figure 4. FTIR spectra of the (a) as-prepared and (b) synthesized samples from RH.

The SEM micrographs for Fe-doped SiO_2 calcined at 400°C (Figure 5a) and AnS (Figure 6) showed similarly sized grains that exhibit smooth surfaces. From visual inspection, average grain size diameter is 0.6-1.4 μm for AnS, 1-2 μm for 5%400RH and 1.5-2.5 μm for 10%400RH.

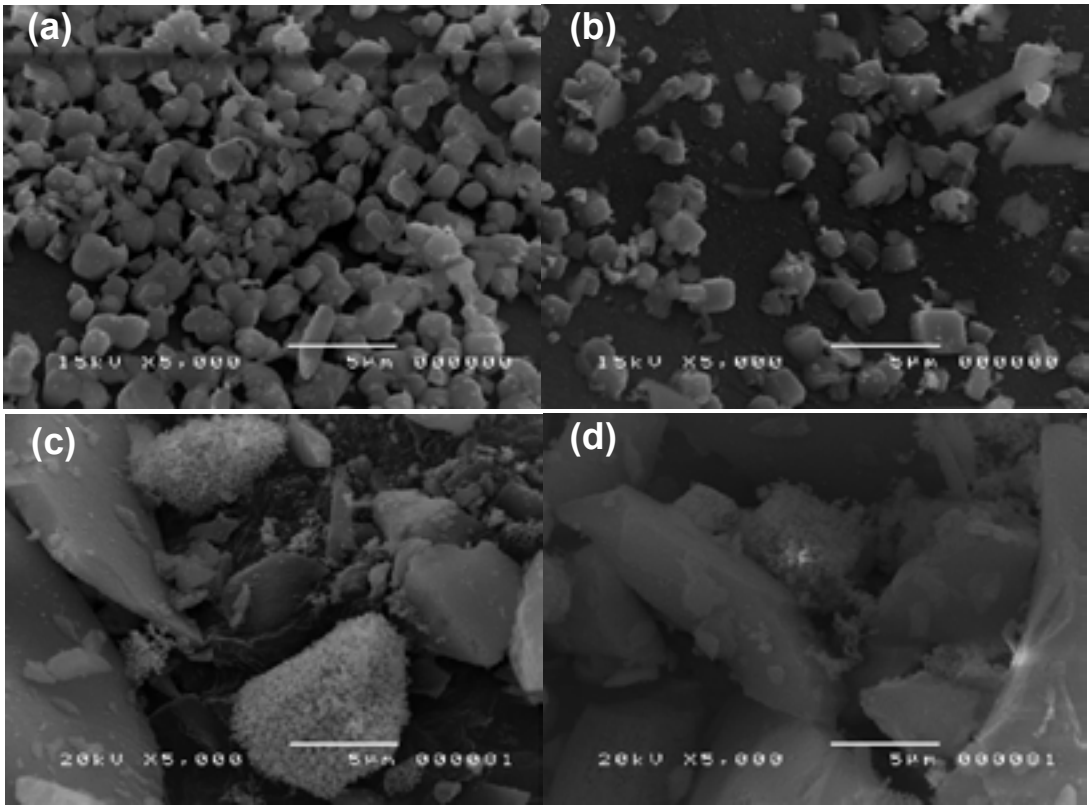

Figure 5. SEM micrograph of (a) 5%-doped RH calcined at 400°C, (b) 10%-doped RH calcined at 400°C, (c) 5%-doped RH calcined at 800°C and (d) 10%-doped RH calcined at 800°C.

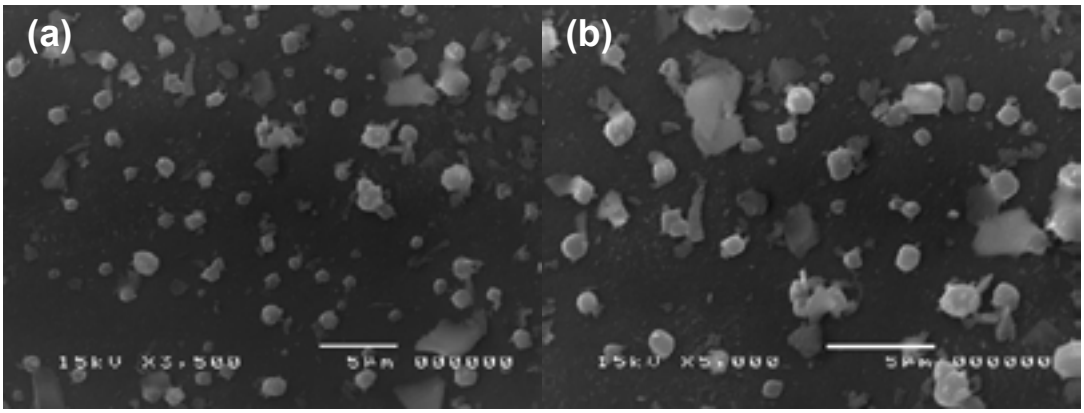

Figure 6. SEM micrographs of AnS calcined at 650°C at (a) 3.5k and (b) 5k magnification.

Fe-doped samples calcined at 800°C (Figure 5c and Figure 5d) showed larger crystal formations, as supported by the increase in XRD diffraction peaks (Figure 3). Space cavities can also be seen on the surface of the grains that were visibly lacking in the samples calcined at 400°C (Figure 5a and Figure 5b). The presence of such cavities can be attributed to the degradation and evaporation of carbonous and combustible residues that were removed when the calcination temperature was increased from 400°C to 800°C. However, while the increase in calcination temperature gave the grains more time to form and grow, it made it difficult to determine the average size of the grains.

EDS analysis for AnS (Figure 7) confirmed the complete removal of carbon residues and the successful incorporation of Fe into the SiO_2 matrix (Figure 8 and Figure 9). When the Si:O ratio was 0.53 for AnS, the ratio was reduced to 0.44 in the 5%-doped RH and 0.46 in the 10%-doped RH calcined at 400°C (Figure 8). Fe:Si ratio meanwhile almost doubled from 0.11 for the 5%-doped RH to 0.23 for the 10%-doped RH when calcined at 400°C. On the other hand, Si:O ratio was at 0.52 for the 800°C-calcined 5%- and 10%-doped samples where the Fe:Si ratio was still 0.11 for the 5%-doped RH and 0.16 for the 10%-doped RH (Figure 9).

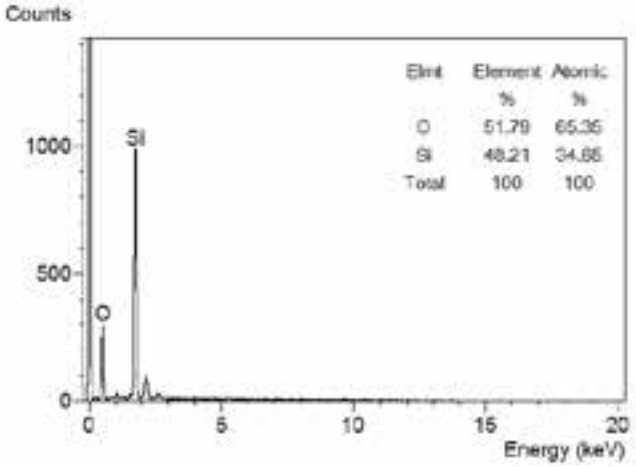

Figure 7. EDS spectra and elemental analysis of AnS calcined at 650°C.

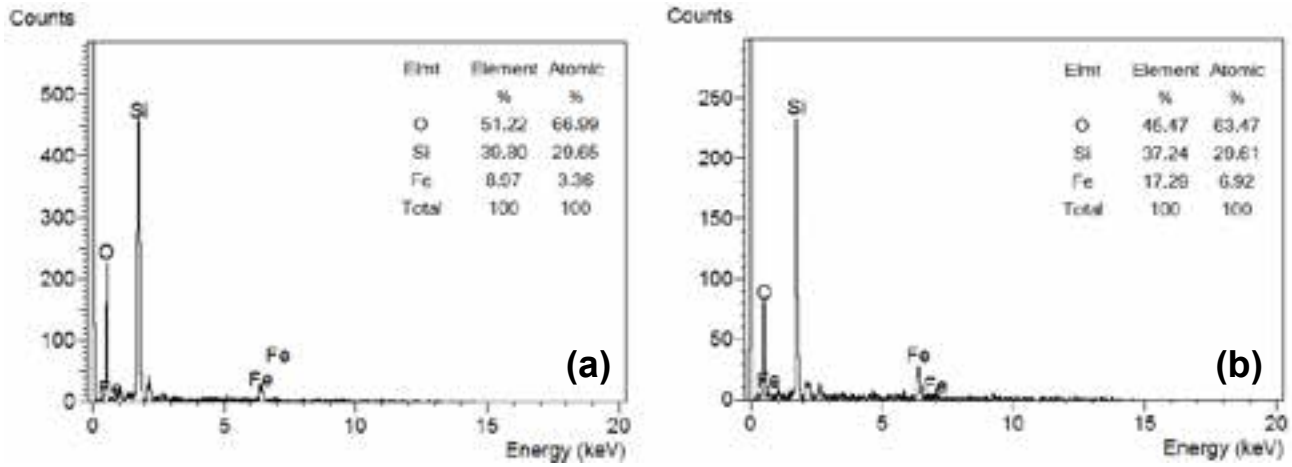

Figure 8. EDS pattern and elemental composition of (a) 5%-doped and (b) 10%-doped RH calcined at 400°C.

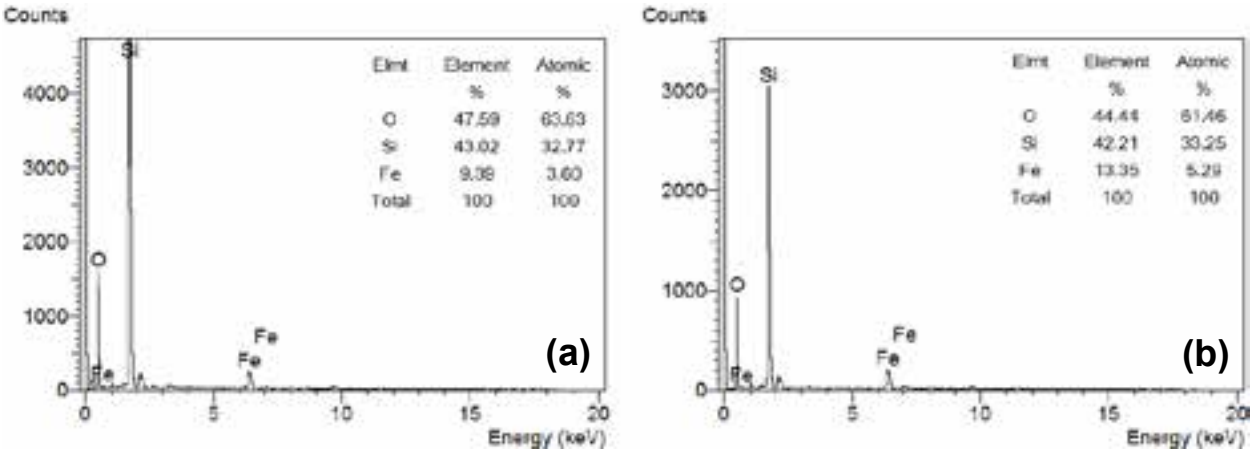

Figure 9. EDS pattern and elemental composition of (a) 5%-doped and (b) 10%-doped RH calcined at 800°C.

Electrochemical Characterization Results

Table 2 summarizes the lithiation and delithiation capacities, and shows comparable CEs for RH calcined at 400°C and 800°C. Average open-circuit values (OCV) for the four RH-sourced samples was calculated at 2.715V. From the presented values, OCV varies with calcination temperature and iron doping. The results indicated an increase in OCV with an increase in calcination temperature. Increasing the amount of iron, meanwhile, resulted in decreased OCV. The potential of a fuel cell is the combination of all electrochemical reaction potentials or mixed potentials that take place within the system. Increasing the amount of iron dopant could possibly increase the formation of impurities brought about by side reactions that could eventually lead to the decrease in the system's potential. On the other hand, when calcination temperature was increased, side reactions were suppressed and may have also caused increased exchange current density in the system.

From Figure 10a, increasing the calcination temperature from 400°C to 800°C resulted in an increase in the lithiation capacity due to the decrease of impurities. Increasing the amount of Fe-doping produced mixed results in lithiation capacities. Likewise, increasing the doping of samples calcined at 400°C showed great increase in its lithiation capacity. This increase can be

Table 2. First cycle charge/discharge capacities and CEs of Fe-doped SiO_2 samples from RH subjected to a constant current of 0.05 mA.

Sample	OCV, V	C-rate	Lithiation Capacity, $mAh \cdot g^{-1}$	Delithiation Capacity, $mAh \cdot g^{-1}$	Coulombic Efficiency, %
5%400RH	2.835	0.012C	395.87	58.63	14.81
5%800RH	2.916	0.014C	959.52	238.58	24.86
10%400RH	2.343	0.020C	780.28	9.74	1.25
10%800RH	2.766	0.016C	787.47	203.47	25.84

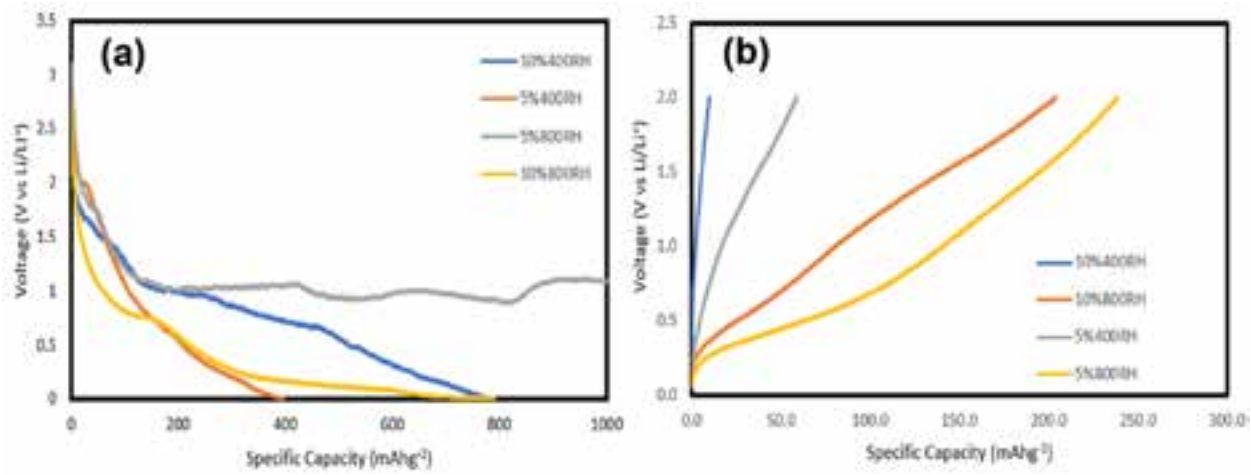

Figure 10. (a) Lithiation and (b) delithiation specific capacities of 5%- and 10%-doped SiO_2 samples from RH calcined at 400°C and 800°C subjected to a constant current of 0.05 mA.

attributed to the increase of participating Fe^{2+}/Fe^{3+} in the redox reaction. On the other hand, an increase in the amount of Fe-doping in samples calcined at 800°C only resulted in a slight decrease of lithiation capacity.

The trend in delithiation specific capacities of samples calcined at 400°C and 800°C (Figure 10b) also supports the data presented earlier. An increased calcination temperature for both 5%- and 10%-doped samples resulted in increased delithiation capacities. This rise can be accounted by the reduction of impurities in the sample. It is clear in the delithiation graphs that increasing the doping content of SiO_2 from 5% to 10% resulted in a decreased delithiation capacity of the sample. Overall, the 5%-doped RH sample calcined at 800°C showed the highest lithiation and delithiation capacity.

The main purpose of the anode materials synthesized in the study is to receive lithium-ion during charging and emit lithium-ion during discharging. The results demonstrated the capacity of this electrode material to perform these Li-ion exchanges, thus manifesting the potential as anode material for LIBs. Doping silica with a metallic material, such as Fe, has therefore provided synergistic effects. The good mean ionic and electronic conductivity of silicon and iron may have led to the increased lithium storage capacity of the anode material.

Conclusion

Fe-doped, mainly amorphous SiO_2 was successfully synthesized from waste RH. TG-DTA showed a total weight loss of 89% where an increase in calcination temperature from 400°C to 800°C has shown decreased residual impurities. XRD patterns of RH-sourced samples revealed a combination of amorphous and crystalline peaks. FTIR results for all synthesized samples showed the three characteristic absorption bands arising from the Si-O-Si groups at approximately 460 cm^{-1}, 800 cm^{-1} and 1020–1110 cm^{-1}. Both FTIR and XRD of samples confirmed the reduction of combustible residuals with increasing calcination temperature (400°C-800°C). The SEM micrographs of pure and doped SiO_2 from RH calcined at 400°C showed similarly-sized individual spherical grains that exhibit a smooth surface. Samples calcined at 800°C, meanwhile, looked like an aggregation of nano-particles with internal void spaces.

From this research, the combination of an amorphous and crystalline doped sample promoted better anode performance as compared to a purely amorphous doped sample. Also, obtaining purely crystalline SiO_2 from RH may need a temperature higher than 800°C, as calcining at this temperature still produces crystals with amorphous grains. GCD results

have shown that 5% rice hull calcined at 800°C indicated both lithiation and delithiation capacities for the doped samples. It suggests that increasing the calcination temperature from 400°C to 800°C greatly increased the ionic conductivity of silica obtained from rice hull. On the other hand, increasing the amount of dopant from 5% to 10% decreased both lithiation and delithiation capacities. Overall, the study has presented the potential of using doped silica rice hull as an electrode material for LIBs.

Acknowledgments

This study was financially supported by Philippine Council for Industry, Energy, and Emerging Technology Research and Development of the Department of Science and Technology (PCIEERD-DOST).

References

Adams, F., Ikotun, B., Patrick, D., & Mulaba-Bafubiandi, A. (2013). Characterization of rice hull ash and its performance in turbidity removal from water. *Particulate Science and Technology 32*(4), 329-333.

Bansal, V., Ahman, A., & Sastry, M. (2006). Fungus mediated biotransformation of amorphous silica in rice husks to nanocrystalline silica. *Journal of American Chemical Society*, *128*(43), 14059-14066.

Bhanvase, B., & Pawade, V. (2018). Advanced nanomaterials for green energy: Current status and future perspectives. In B. Bhanbase et al. (Eds.), *Nanomaterials for Green Energy*. Amsterdam: Elsevier.

Caldona, E.B., de Leon, A.C.C., Thomas, P.G., Naylor III, D.F., Pajarito, B.B., & Advincula, R.C. (2017). Superhydrophobic Rubber-Modified Polybenzoxazine/SiO_2 Nanocomposite Coating with Anticorrosion, Anti-Ice, and Superoleophilicity Properties. *Industrial & Engineering Chemistry Researc*h, *56*(6), 1485-1497.

Caldona, E.B., Sibaen, J.W., Tactay, C.B., Mendiola, S.L.D., Abance, C.B., Anes, M.P., Serrano, F.D.D., & de Guzman, M.M.S. (2019). Preparation of Spray-Coated Surfaces from Green-Formulated Superhydrophobic Coatings. *Applied Sciences 1, 12*, 1657.

Cervera, R.B., Suzuki, N., Ohnishi, T., Osada, M., Mitsuishi, K., Kambara, T., & Takada, K. (2014). High performance silicon-based anodes in solid-state lithium batteries. *Energy & Environmental Science, 7*(2), 662-666.

Chakraverty, A., Mishra, P., & Banerjee H.D. (1985). Investigation of thermal decomposition of rice husk. *Thermochima Acta, 94*, 267-275.

Chang, W., Park, C., Kim, J., Kim, Y., Jeong, G., & Sohn, H. (2012). Quartz (SiO_2): a new energy storage anode material for Li-ion batteries. *Energy & Environmental Science, 5*, 6895-6899.

Cui, J., Cheng, F., Lin, J., Yang, J., Jiang, K., Wen, Z., & Sun, J. (2017). High surface area C/SiO_2 composites from rice husks as a high-performance anode for lithium ion batteries. *Powder Technology, 311*, 1-8.

Dai, F., Yi, R., Gordin, M.L., Chen, S., & Wang, D. (2012). Amorphous Si/SiOx/SiO_2 nanocomposites via facile scalable synthesis as anode materials for Li-ion batteries with long cycling life. *RSC Advances, 2*(33), 12710.

Ferreira, C.S., Dos Santos, P.L., Bonacin, J., Passos, R.R., & Pocrifka, L. (2015). Rice husks reuse in the preparation of SnO_2/SiO_2 nanocomposites. *Materials Research, 18*(3), 639-643.

Garrido, C., & Cervera, R. (2015). Synthesis of amorphous Fe-doped SiO_2 anode nanomaterial via sol-gel method. *Advanced Materials Research, 1119*, 38-42.

Genieva, S., Tumanova, S., Dimitrova, A., & Vlaev, L. (2008). Characterization of rice husks and the products of its thermal degradation in air or nitrogen atmosphere. *Journal of Thermal Analysis and Calorimetry, 93*(2), 387-396.

Jin, Y., Zhu, B., Lu, Z., Liu, N., & Zhu, J. (2017). Challenges and Recent Progress in the development of Si anodes for lithium-ion battery. *Advanced Energy Materials, 7*, 1700715.

Ju, Y., Tang, J.A., Zhu, K., Meng, Y., Wang, C., Chen, G., Wei, Y., & Gao, Y. (2016). SiO_x/C composite from rice husks as an

anode material for lithium-ion batteries. *Electrochimica Acta 191*, 411-416.

Hossain, S.S., Mathur, L., & Roy, P.K. (2018). Rice husk/rice husk ash as an alternative source of silica in ceramics: A review. *Journal of Asian Ceramic Societies, 6*(4), 299-313.

Kim, H.J., Choi, J.H., & Choi, J.W. (2017). Rice husk-originating silicon–graphite composites for advanced lithium ion battery anodes. *Nano Convergence, 4*(1), 24.

Li, J. (2012). Understanding degradation and lithium diffusion in lithium ion battery electrodes (Unpublished doctoral dissertation). University of Kentucky, Lexington, Kentucky.

Liou, T.H., & Yang, C.C. (2011). Synthesis and surface characteristics of nanosilica produced from alkali-extracted rice husk ash. *Materials Science and Engineering: B, 176*(7), 521-529.

Liu, H., Guo, Z., Wang, J., & Konstantinov, K. (2010). Si-based anode materials for lithium rechargeable batteries. *Journal of Materials Chemistry, 20*(45), 10055.

Liu, N., Huo, K., McDowell, M., Zhao, J., & Cui, Y. (2013). Rice husks as a sustainable source of nanostructured silicon for high performance Li-ion battery anodes. *Scientific Reports, 3*, 1919.

Liu, X., & Huang, J.Y. (2011) In situ TEM electrochemistry of anode materials in lithium ion batteries. *Energy & Environmental Science, 4*, 3844-3860.

Ma, D., Cao, Z., & Hu, A. (2014). Si-based anode materials for Li-ion batteries: A mini review. *Nano-Micro Letters, 6*(4), 347–358.

Ma, X., Zhang, M., Liang, C. Li, Y., Wu, J., & Che, R. (2015). Inheritance of crystallographic orientation during lithiation/delithiation processes of single-crystal α-Fe_2O_3 nanocubes in lithium-ion batteries. *ACS Applied Materials & Interfaces, 7*(43), 24191-24196.

Manthiram, A. (2009). Materials for high-energy density batteries. In S. Priya and D.J. Inman (Eds.), *Energy Harvesting Technologie*s. Germany: Springer.

Mirasol, E., & Cervera, R. (2015). Production of amorphous and crystalline silica from Philippine waste rice hull. *Advanced Materials Research, 1098*, 80-85.

Mukanova, A., Jetybayeva, A., Myung, S., Kim, S., & Bakenov, Z., (2018). Amini-review on the development of Si-based thin film anodes for Li-ion batteries. *Materials Today Energy, 9*, 49-66.

Music, S., Filipovic-Vincekovic, N., & Sekovanic L. (2011). Precipitation Of Amorphous SiO_2 Particles And Their Properties. *Brazilian Journal of Chemical Engineering, 28*, 89-94.

Ong, H.R., Iskandar, W.M., & Khan, M.R. (December 24th 2019). Rice Husk Nanosilica Preparation and Its Potential Application as Nanofluids [Online First], IntechOpen, DOI: 10.5772/intechopen.89904. Available from: https://www.intechopen.com/online-first/rice-husk-nanosilica-preparation-and-its-potential-application-as-nanofluids

Park, C.M., Kim, J.H., Kim, H., & Sohn, H.J. (2010) Li-alloy based anode materials for Li Secondary batteries. *Chemical Society Reviews, 39*(8), 3115-3141.

Phonphuak, N. & Chindaprasit, O. (2015). Type of waste, properties, and durability of pore-forming waste-based fired masonry bricks. In F. Pacheco-Torgal et al. (Eds.), *Eco-Efficient Masonry Bricks and Blocks*. Amsterdam: Elsevier.

Prado, K., & Spinace, M. (2015). Characterization of fibers from pineapple's crown, rice husks and cotton textile residues. *Materials Research, 18*(3), 530-537.

Sethurma, V., Srinivasan, V., & Newman, J. (2012). Analysis of electrochemical lithiation and delithiation kinetics in silicon. *Journal of Electrochemical Society, 160*(2), A394-A403.

Wang, W., Martin, J., Zhang, N., Ma, C., Han, A., & Sun, L. (2011). Harvesting silica nanoparticles from rice husks. *Journal of Nanoparticle Research, 13*(12), 6981-6990.

Wen, Z., Lu, G., Mao, S., Kim, H., Cui, S., Yu, K., Huang, X., Hurley, P.T., Mao, O.O., & Chen, J. (2013). Silicon nanotube anode for lithium-ion batteries. *Electrochemistry Communications, 29*, 67-70.

Wu, Y., Wang, W., Ming, J., Li, M., Xie, L., He, X., Wang, J., Liang, S., & Wu, Y. (2019). An exploration of new energy storage system: High energy density, high safety, and fast charging lithium ion battery. *Advanced Functional Materials, 29*(1), 1-7.

Yin C., & Goh, B. (2011). Thermal degradation of rice husks in air and nitrogen: thermogravimetric and kinetic analyses. *Energy Sources, Part A: Recovery, Utilization, and Environmental Effects, 34*, 246-252.

Zhang, J., Lu, B., Song, Y., & Ji, X. (2012). Diffusion induced stress in layered Li-ion battery electrode plates. *Journal of Power Sources, 209*, 220-227.

Zhao, K., Tritsaris, G.A., Pharr, M., Wang, W.L., Okeke, O., Suo, Z., & Kaxiras, E. (2012) Reactive flow in silicon electrodes assisted by the insertion of lithium. *Nano Letters, 12*(8), 4397-4403.